<u>Supplementary Material</u>

Ultra-high pressure disordered eight-coordinated phase of Mg$_2$GeO$_4$: Analogue for super-Earth mantles

Rajkrishna Dutta[1, 2*], Sally J. Tracy[1], R. E. Cohen[1], Francesca Miozzi[1], Kai Luo[1], Jing Yang[1], Pamela C. Burnley[3], Dean Smith[4], Yue Meng[4], Stella Chariton[5], Vitali B. Prakapenka[5], and Thomas S. Duffy[2]

[1]Earth and Planets Laboratory, Carnegie Institution for Science, Washington DC 20015 USA.
[2]Department of Geosciences, Princeton University, Princeton, NJ 08544 USA.
[3]Department of Geoscience, University of Nevada, Las Vegas, NV 89154 USA.
[4]HPCAT, X-Ray Science Division, Argonne National Laboratory, Argonne, IL 60439 USA.
[5]Center for Advanced Radiation Sources, The University of Chicago, Chicago, IL 60637 USA.

Contents

S1. Predicted phase boundaries for Mg₂GeO₄ and Mg₂SiO₄ at multi-megabar pressures

Fig. S1. Theoretically calculated phase boundaries (1, 2) for Mg_2SiO_4 (grey line) and Mg_2GeO_4 (black line). Orange and blue squares show the pressure-temperature conditions expected at the core-mantle boundaries of terrestrial- and water-rich exoplanets, respectively (3). The numbers in each square represent the mass of the planet as a multiple of Earth's mass. The shaded region represents the P, T range of this study. The question mark indicates the possible stability region of Th₃P₄-type Mg_2SiO_4. Modified after Umemoto et al., 2017, 2021.

3
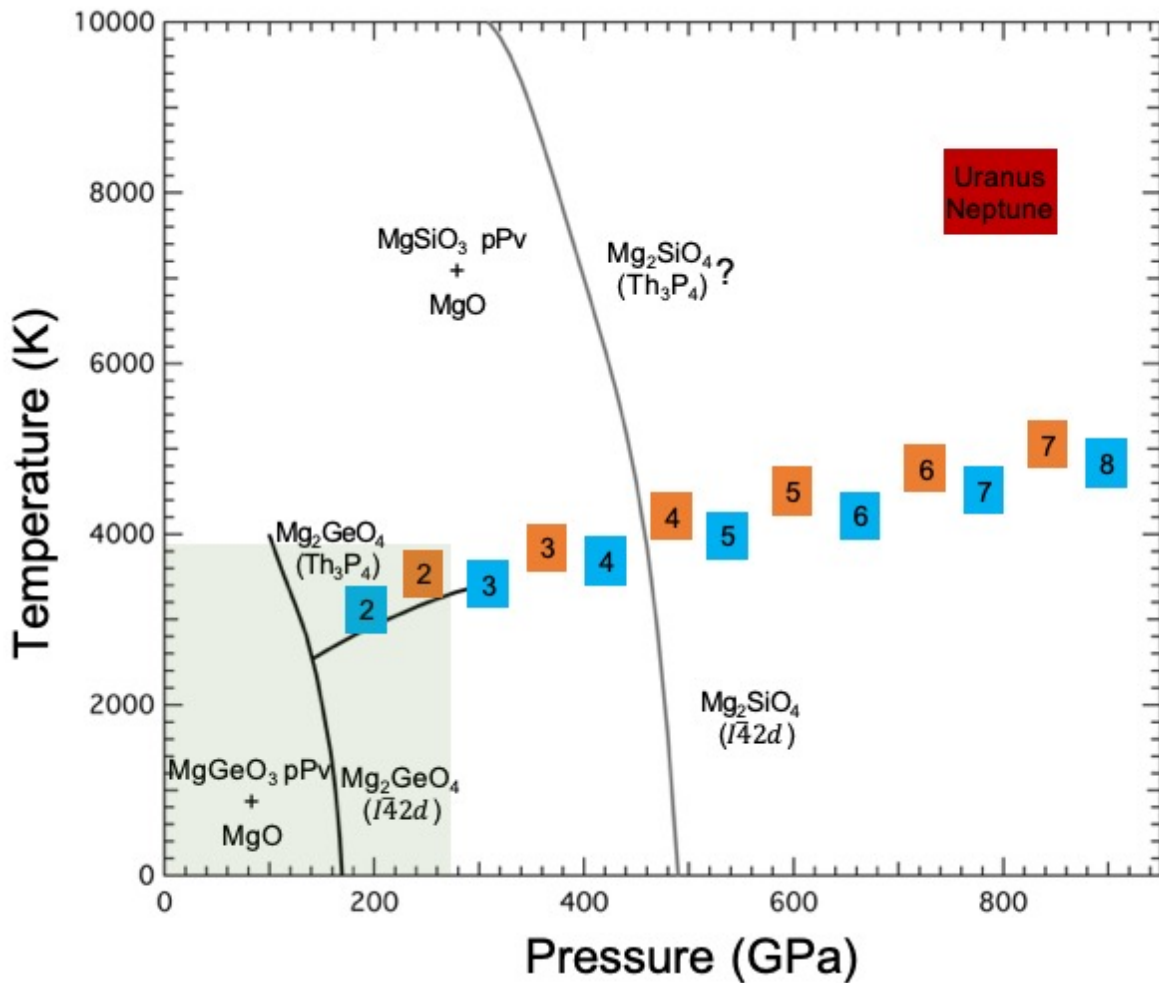
S2. Summary of experiments

Table S1. Summary of the experimental conditions and results

Run. No	Pressure (GPa)	Peak Temperature (K)	Heating duration (min: sec)	Phase(s) Before Heating	Phase(s) Observed During Heating
H1	115	2966 ± 186	26: 42	Amorphous	pPv
G1	134	2751 ± 118	25:47	Amorphous	$Th_3P_4 (\downarrow) + pPv (\uparrow)$
G2	151	2938 ± 69	13:09	Amorphous	$Th_3P_4 (\downarrow) + pPv (\uparrow)$
H2	153	2468 ± 243	10:05	Amorphous	$Th_3P_4 (\downarrow) + pPv (\uparrow)$
H3	160	1806 ± 184	13:47	Amorphous	Th_3P_4
G3	169	3232 ± 185	11:12	Amorphous	$Th_3P_4 (\downarrow) + pPv (\uparrow)$
H2_2	175	3628 ± 382	21:12	$Th_3P_4 + pPv$	$pPv (\downarrow) + Th_3P_4 (\uparrow)$
H4	187	3032 ± 113	13:32	Amorphous	Th_3P_4
H3_2	234	3650 ± 191	17:05	Th_3P_4	Th_3P_4
H3_3	261	2025 ± 45	07:21	Th_3P_4	Th_3P_4

pPv – $MgGeO_3$ post-perovskite phase; Th_3P_4 – thorium phosphide-type Mg_2GeO_4 phase. Upward and downward pointing arrows indicate that the diffraction peaks of the given phase grew or diminished, respectively, as the heating temperature and/or time was increased. The growth of one phase and reduction of another is used to identify the stable phase as low reaction rates under these conditions prevent complete transformation on the timescale of the heating experiments.

S3. Additional computational details

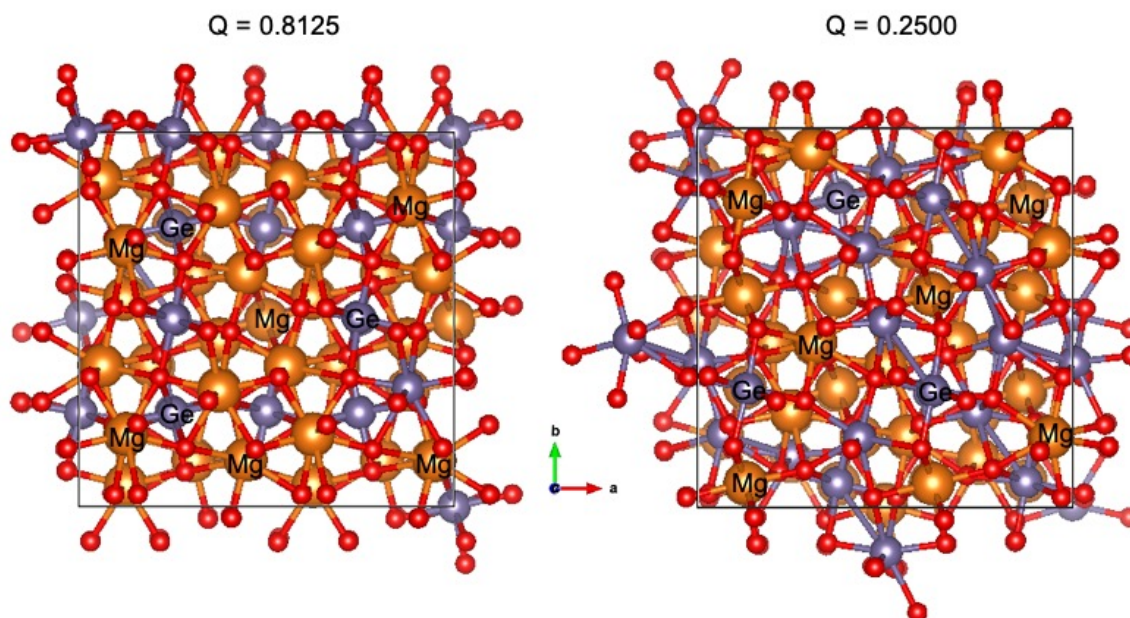**Fig. S2** 224 atoms supercell for $I\bar{4}2d$-Mg$_2$GeO$_4$ at 200 GPa for selected Q values.
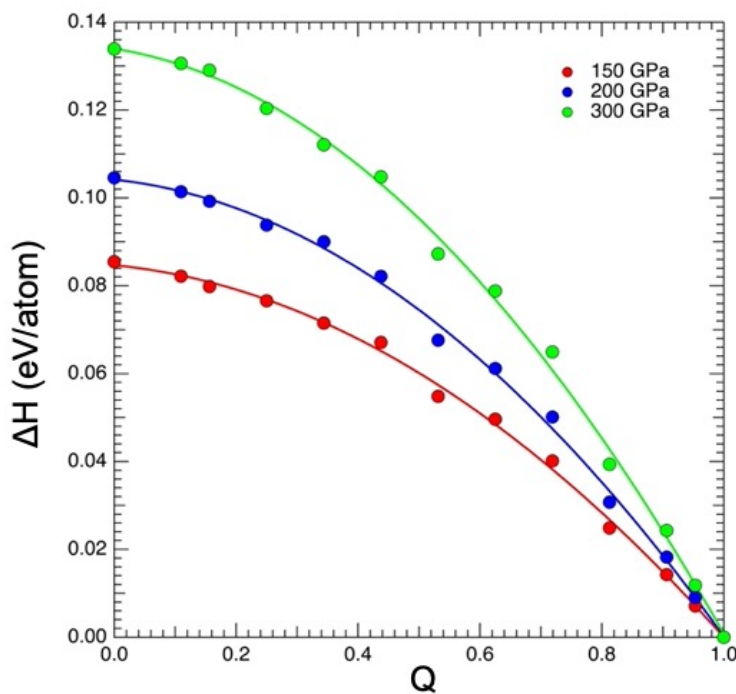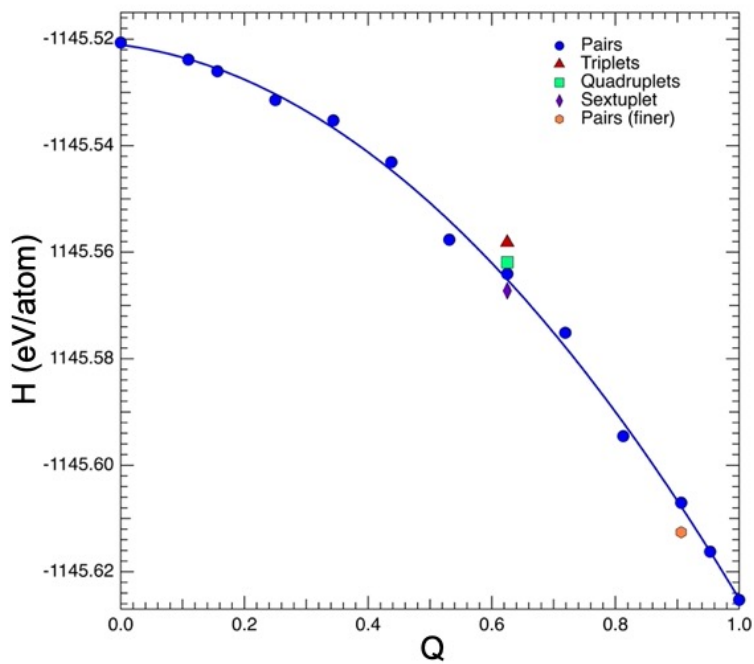

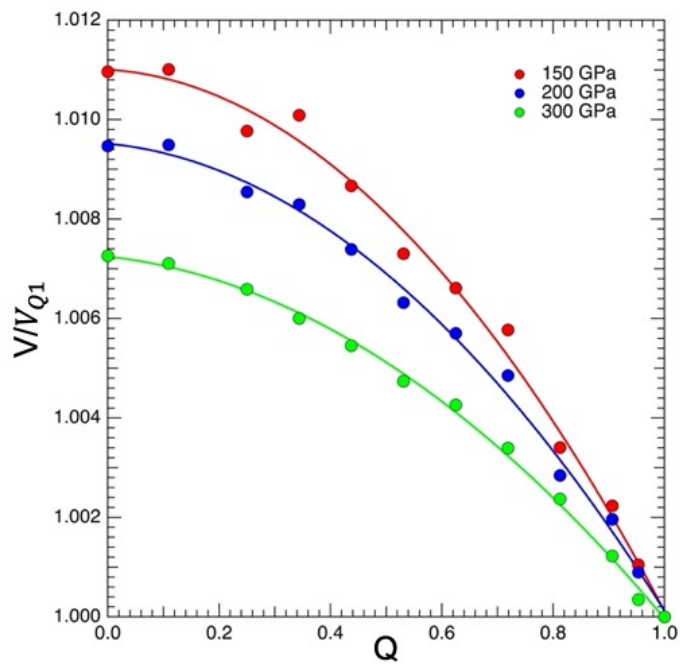**Fig. S3** ΔH ($H_Q - H_{Q1}$) as a function of order parameter, Q at 150 (red), 200 (blue) and 300 (green) GPa; where H_{Q1} is the enthalpy at $Q = 1$.
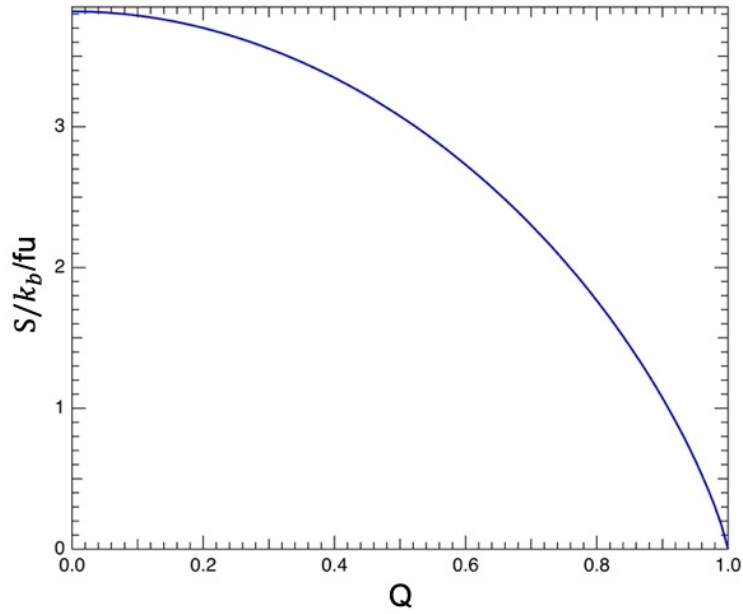
Fig. S4 Change in Enthalpy with order parameter Q for finer convergence criteria and different cluster sizes for selected Q values at 200 GPa.

Fig. S5 Variation in unit cell volume with order parameter Q at 150, 200 and 300 GPa.

Fig. S6 Configurational entropy versus order parameter Q at 200 GPa.

Fig. S7 Gibbs free energy of the completely disordered $I\bar{4}3d$- Mg_2GeO_4 relative to the completely ordered $I\bar{4}2d$-phase at different temperatures. The dashed grey line indicates $\Delta G = 0$, shows the temperature of the $I\bar{4}2d$ to $I\bar{4}3d$ transition at the relevant pressure.
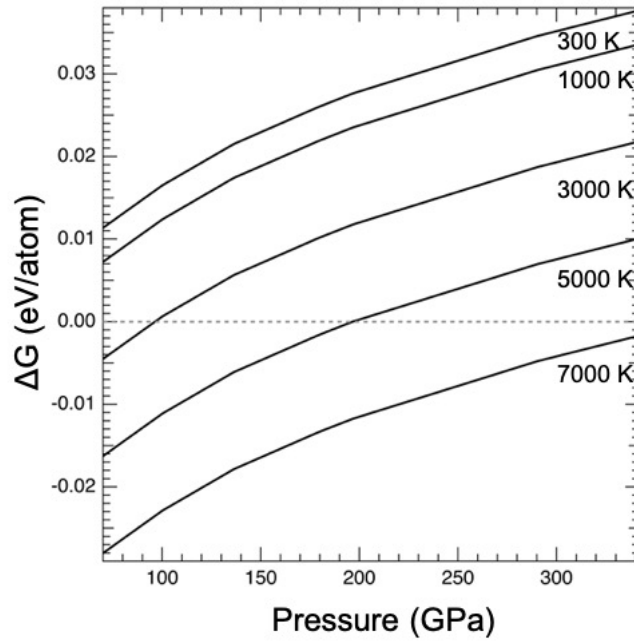
S4. Structure and crystal chemistry of the Th_3P_4-type phase

The Th_3P_4 structure was originally described by Meisel (1939) (4) and Kripyakevich (1963) (5). It is based on a body-centered-cubic lattice with the cations in eight-fold coordination. The structure is intrinsically disordered with both cations occupying the same crystallographic site. There is a single positional parameter, x. The nearest-neighbor cation-anion bond distances are identical when x adopts its ideal value, 1/12. The cation polyhedra are in the form of a strongly distorted cube (octaverticon) with triangular faces. Each anion is bonded to six cations in a distorted octahedron.

The Th_3P_4-type structure occurs commonly in binary chalcogenides of the light rare earth elements in both defective (A_2X_3) and non-defective forms (A_3X_4), often exhibiting solid solutions between them (6). It also occurs widely in ternary AB_2X_4 chalcogenides where A is a divalent metal cation and B is a light rare earth element (7, 8). Its prevalence in light rare earths indicate the structure is favored by compounds with a large ratio of cation to anion radius. Based on AB_2X_4 structure maps (7, 8), the phase is favored in compounds in which the radii of the cations, r_A and r_B, are similar ($r_A/r_B \sim 0.8 - 1.2$) and have low electronegativity. At larger cation radius ratios, the calcium ferrite-type structure ($CaFe_2O_4$) is preferred instead. Chalcogenides with the Th_3P_4 structure have attracted interest for technical applications because the structure is highly flexible and can incorporate many types of impurities and defects (9). At high pressures and temperatures, ternary sulfospinels AB_2S_4 (A=Mg, Mn, B=Tm, Yb) have been shown to transform to the Th_3P_4-type structure (10). The structure has also been synthesized at high pressure in nitrides including Hf_3N_4, Zr_3N_4, and Ti_3N_4, in which the phase is found to be highly incompressible (11, 12). The structure can also describe an electride phase in alkali metals formed at high pressure (13).

Fig. S8. Comparison of the observed diffraction pattern (black) for Mg_2GeO_4 at 187 GPa, 2010 K with the theoretically calculated $I\bar{4}2d$-type phase (green ticks; $a = 5.417$ Å and $c = 5.592$ Å at 197 GPa) and the $I\bar{4}3d$-type structure (red ticks; $a = 5.492$ Å at 193 GPa). Miller indices of Th_3P_4-type (red) Mg_2GeO_4 are listed above each peak. Red and green curves show the fit and background, respectively. Peaks labeled Re and Au are from rhenium gasket and gold pressure marker, respectively.
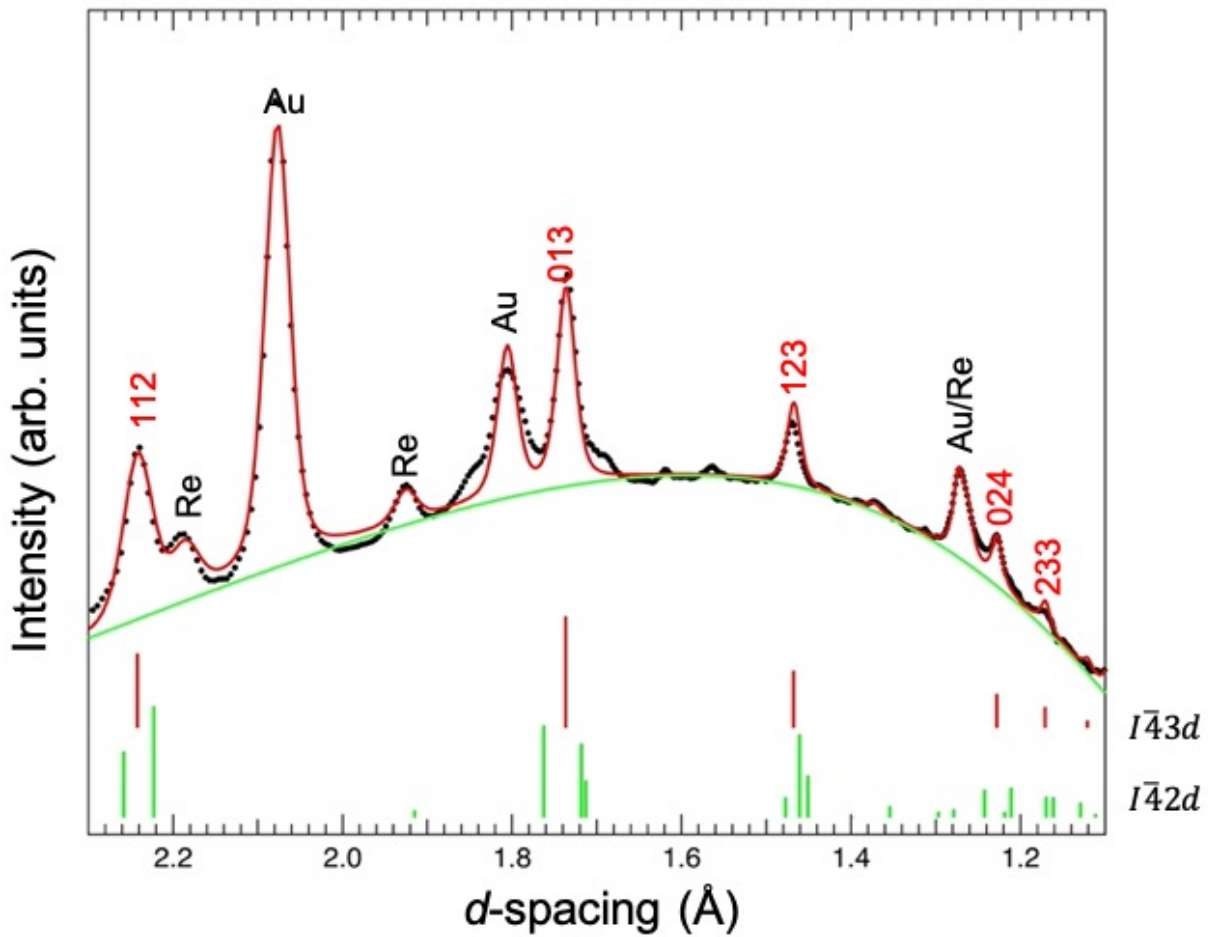
Table S2. Calculated and observed d-spacings of Th_3P_4-type Mg_2GeO_4 obtained after heating to 3650 K at 240 GPa and then quenching to room temperature. The lattice parameter is $a = 5.4055$ (7) Å. The unit cell dimension is in excellent agreement with that obtained from a Rietveld refinement of the same pattern, $a = 5.4055$ (2) Å.

h	k	l	d-observed (Å)	d-calculated (Å)	Δd (Å)
1	1	2	2.2064	2.2068	-0.0004
0	1	3	1.7090	1.7093	-0.0003
1	2	3	1.4462	1.4446	0.0016
0	2	4	1.2079	1.2087	-0.0008
2	3	3	1.1525	1.1524	0.0001

Table S3. Structural parameters of the Th_3P_4-type Mg_2GeO_4 from experiments and DFT computations.

|	Experiment	Theory*
Pressure (GPa)	184	193
a (Å)	5.4930 (7)	5.492
Mg/Ge coordinate (12a)	(0.375, 0, 0.25)	(0.375, 0, 0.25)
O coordinate (16b)	(0.055, 0.055, 0.055)	(0.0646, 0.0646, 0.0646)
Ge-O (Å)	1.745	1.796
Mg-O (Å)	2.080	2.015

*Theoretical calculations correspond to 0 K while experiments correspond to 300 K

S5. Additional X-ray diffraction results for the Th₃P₄-type phase of Mg₂GeO₄

Fig. S9. X-ray diffraction patterns obtained on a sample heated at 158 GPa (H3) followed by subsequent cold compression and heating at 240 GPa (Run H3_2). The pattern at the bottom in grey shows the pattern obtained on quenching Mg_2GeO_4 after heating to 1806 K at 158 GPa showing weak peaks of the Th_3P_4 phase (indicated by red circles) formed metastably at this pressure. The upper traces (black) show a series of diffraction patterns at increasing temperature for the heating cycle at 240 GPa (H3_2). The peaks of the Th_3P_4 phase grow with temperature upon heating to as high as 3650 K, which supports the stability of the Th_3P_4 phase at these P-T conditions.
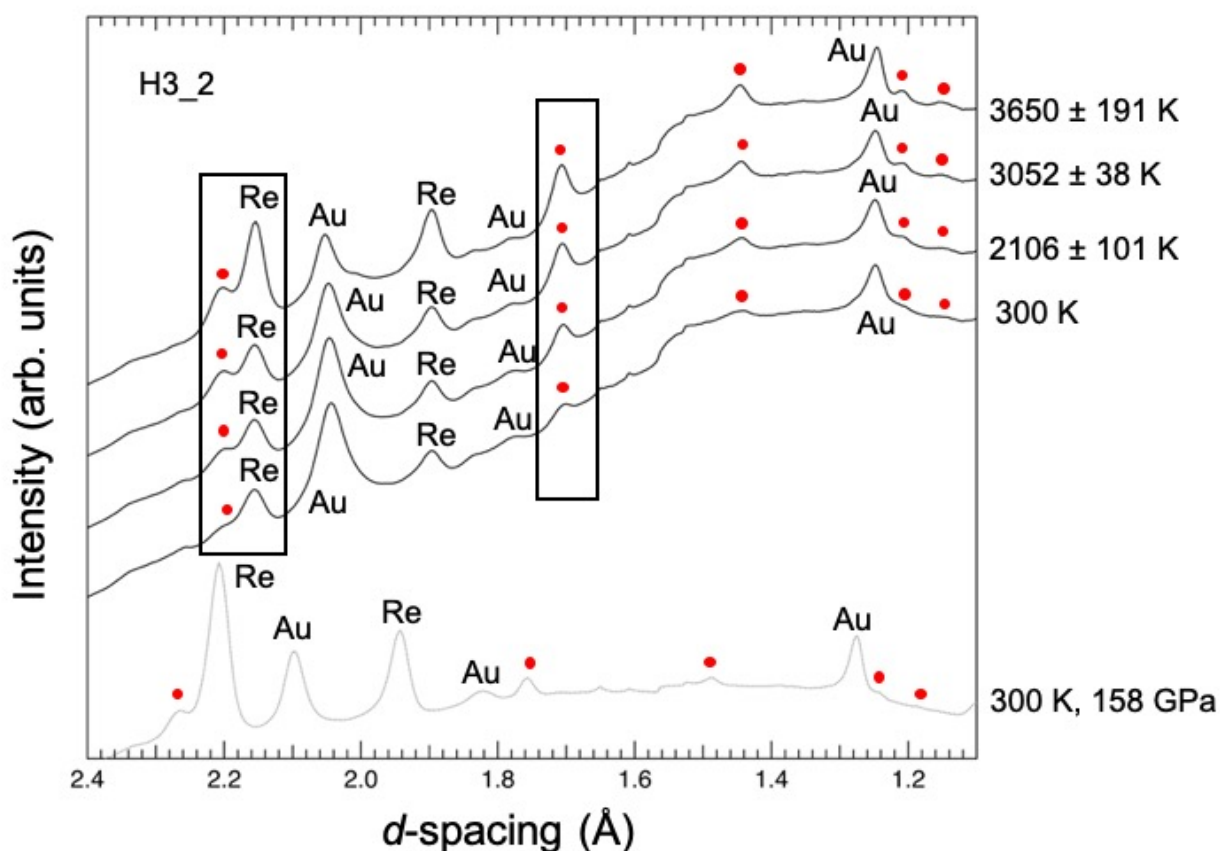
Fig. S10. Two-dimensional diffraction image of Mg_2GeO_4 after heating to 3650 K at 240 GPa with subsequent quenching to room temperature. The left figure shows the raw image, which is transformed to coordinates of azimuthal angle around the X-ray beam vs. two-theta in the right-hand image. The integrated one-dimensional pattern for this image is shown in Fig. 3. Arrows (yellow: Au, light blue: Re, and purple: Th_3P_4-type Mg_2GeO_4) show the peak positions in the integrated pattern.
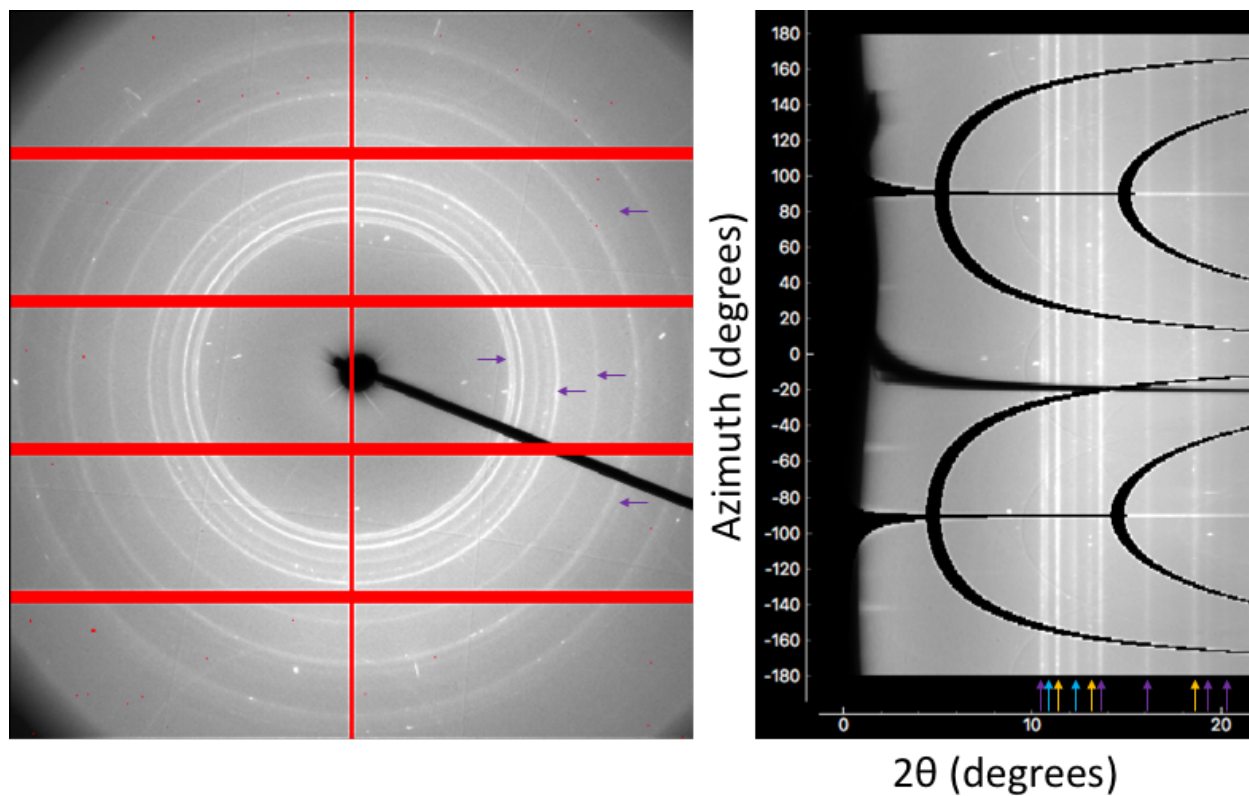
S6. Additional X-ray diffraction results for the post-perovskite phase of MgGeO₃

Fig. S11. X-ray diffraction patterns during the heating cycle at 115 GPa (H1). Brown circles indicate post-perovskite peaks. The total heating duration was 11 minutes 21 seconds with ~1-1.5 minutes at each step.
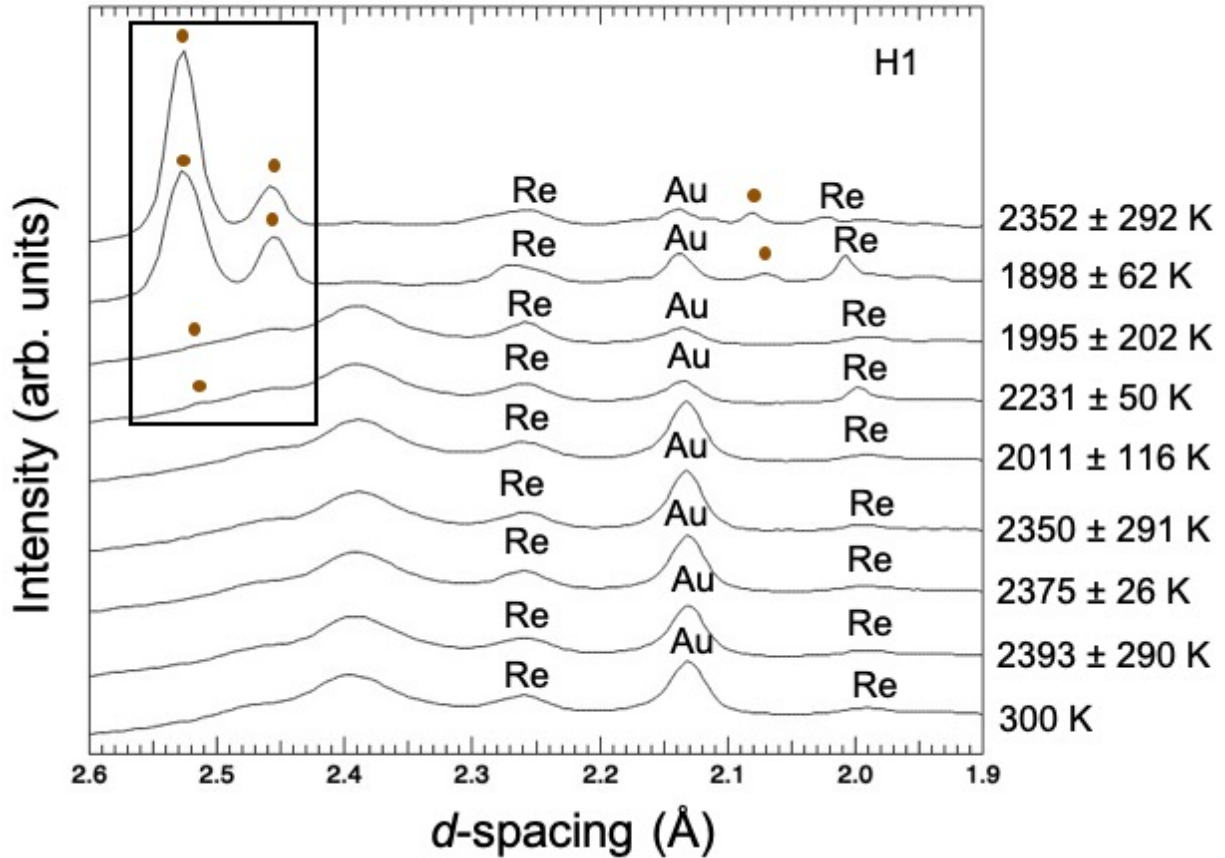
Fig. S12. X-ray diffraction pattern obtained after heating Mg_2GeO_4 to 3200 K at 179 GPa, followed by quenching to room temperature (quenched P = 172 GPa). The tick marks at the bottom indicate the expected peak positions for Th_3P_4 (red), post-perovskite (brown), gold (yellow), and MgO (blue). Miller indices of pPv-$MgGeO_3$(brown) and Th_3P_4-type (red) Mg_2GeO_4 are listed above each peak.
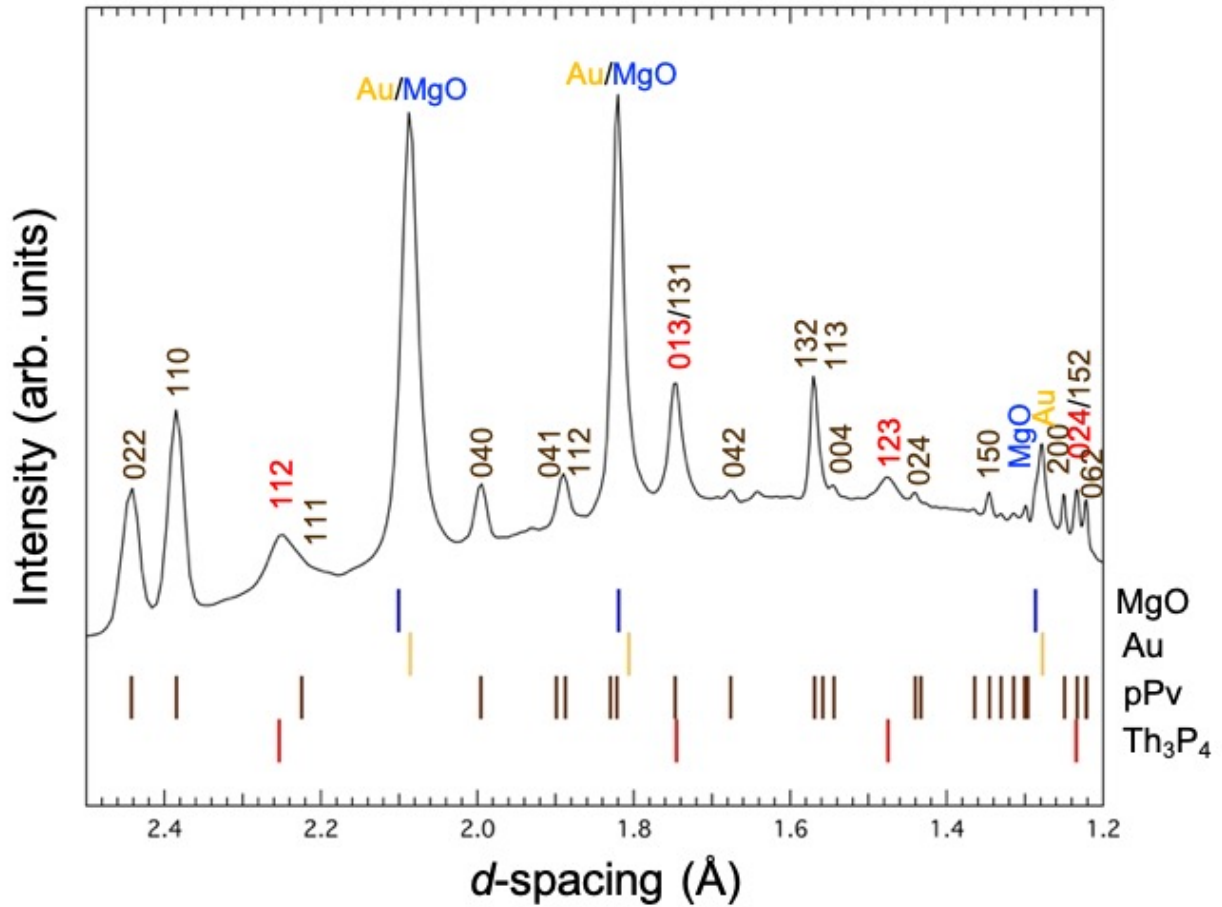
Table S4. Calculated and observed *d*-spacings of post-perovskite MgGeO$_3$ at 172 GPa. The fit lattice parameters are *a* = 2.498 (1) Å, *b* = 7.982 (3) Å, and *c* = 6.177 (4) Å.

h	*k*	*l*	*d*-observed (Å)	*d*-calculated (Å)	Δ*d* (Å)
0	2	0	3.9905	3.9911	-0.0006
0	0	2	3.0869	3.0883	-0.0014
0	2	2	2.4431	2.4425	0.0006
1	1	0	2.3851	2.3847	0.0004
0	4	0	1.9956	1.9955	0.0001
1	3	1	1.7462	1.7471	-0.0009
1	3	2	1.5694	1.5689	0.0005

References

1. K. Umemoto, *et al.*, Phase transitions in $MgSiO_3$ post-perovskite in super-Earth mantles. *Earth Planet. Sci. Lett.* **478**, 40–45 (2017).

2. K. Umemoto, R. M. Wentzcovitch, Ab initio prediction of an order-disorder transition in Mg_2GeO_4: Implication for the nature of super-Earth's mantles. *Phys. Rev. Mater* **5**, 093604 (2021).

3. C. Sotin, O. Grasset, A. Mocquet, Mass–radius curve for extrasolar Earth-like planets and ocean planets. *Icarus* **191**, 337–351 (2007).

4. K. Meisel, The crystal structure of thorium phosphides. *Z. anorg. allgem. Chem* **240** (1939).

5. P. I. Kripyakevich, A structure of the Th_3P_4 type as an arrangement of polyhedrons. *Soviet Phys. Cryst.* **7** (1963).

6. J. Flahaut, *et al.*, *Acta Cryst.* **19**, 14–19 (1965).

7. X. Zhang, A. Zunger, Diagrammatic separation of different crystal structures of A_2BX_4 compounds without energy minimization: a pseudopotential orbital radii approach. *Adv. Funct. Mater*. **20**, 1944–1952 (2010).

8. J. E. Iglesias, H. Steinfink, Crystal chemistry of AB_2X_4 (X = S, Se, Te) compounds. *J. Solid State Chem*. **6**, 119–125 (1973).

9. C. E. Whiting, E. S. Vasquez, C. D. Barklay, Uranium based materials as potential thermoelectric couples for future radioisotope power systems in *2018 IEEE Aerospace Conference*, (2018), pp. 1–9.

10. K. Hirota, N. Kinomura, S. Kume, M. Koizumi, Transition of sulfospinel to Th_3P_4 type phase under pressure. *Mater. Res. Bull*. **11**, 227–232 (1976).

11. A. Zerr, G. Miehe, R. Riedel, Synthesis of cubic zirconium and hafnium nitride having Th_3P_4 structure. *Nat. Mater*. **2**, 185–189 (2003).

12. V. S. Bhadram, *et al.*, Semiconducting cubic titanium nitride in the Th_3P_4 structure. *Phys. Rev. Mater*. **2**, 011602 (2018).

13. C. J. Pickard, R. J. Needs, Predicted pressure-induced s-band ferromagnetism in alkali metals. *Phys. Rev. Lett*. **107**, 087201 (2011).